The International Archives of the Photogrammetry, Remote Sensing and Spatial Information Sciences, Volume XLIX-B2-2026
XXV ISPRS Congress 2026 “From Imagery to Understanding”, Commission II, 4–11 July 2026, Toronto, Canada

A Workflow for the automatic Extraction of Glacier Contours from 4D Point Clouds

Steffen Isfort[1], Melanie Elias[2], Hans-Gerd Maas[1]

[1]Institute of Photogrammetry and Remote Sensing, TUD - Dresden University of Technology, Germany - (steffen.isfort, hans-gerd.maas)@tu-dresden.de
[2]Faculty of Spatial Information, HTWD - University of Applied Sciences Dresden, Germany - melanie.elias@htw-dresden.de

Keywords: glacier margin mapping, geomorphological mapping, rock glacier, multi-temporal point clouds

Abstract

In this paper, we propose a basic workflow for the automatic extraction of glacier contours from high-resolution multi-temporal 3D point clouds. Based on the hypothesis, that glacier movements cause changes in multi-temporal surface models, glacier contours can be detected even in scenarios where glacier margins are not clearly visible, such as in the case of debris-covered glaciers and rock glaciers. After applying a robust registration algorithm, glacier and non-glacier points are filtered in several steps and spatial resolutions based on dense clusters of significantly changed points. Finally, the glacier margin is mapped using a contour extraction algorithm. The method is applied to various datasets in two scenarios: first, to a slightly debris-covered glacier in Norway; second, to a rock glacier in the Austrian Alps. The results clearly demonstrate the basic functionality of the proposed method. However, morphological changes not caused by glacier movement limit the effectiveness of the filtering, which relies exclusively on density-based elevation changes. Against this background, future work will focus on incorporating additional features, such as velocity fields and prior knowledge of rock glacier dynamics, into the point cloud filtering.

1. Introduction

Glaciers in high mountain regions can be considered important climate indicators due to their sensitive interaction with the climate (Gardner et al., 2013; Oerlemans, 1994). The mapping of these glacier margins is primarily based on recording the spectral reflectance signatures of snow and ice in remote sensing images. As highlighted by the literature, a major source of uncertainty is debris cover on the glacier surface (Shangguan et al., 2015; Pfeffer et al., 2014). This limitation applies in particular to rock glaciers, which are by definition debris landforms. Mapping rock glacier margins is a challenging task under research. The primary method is manual assessment of the margins by one or several experts, which can lead to subjective and inconsistent results (Brardinoni et al., 2026). Automatic approaches attempt to overcome these limitations and map the margins of rock glaciers for instance based on velocity fields derived from interferometric synthetic aperture radar (InSAR) measurements (Bertone et al., 2024) or use deep learning in image analysis (Robson et al., 2020).

Our approach aims to determine the glacier margin of both debris-covered glaciers and rock glaciers using multi-temporal, high-resolution 3D point clouds. These can be acquired, for example, through terrestrial laser scanning (TLS) and imagery from unmanned aerial vehicles (UAVs). Both methods are frequently used in glacier research (see for example (Avian et al., 2020), (Ulrich et al., 2021)). Given a robust registration of a pair of multi-temporal point clouds, geomorphologically active areas can be identified through change detection. The hypothesis is, that glacier movements cause changes in the surface models, and thus, change detection between two epochs reveals the glacier contours of the first epoch. The identification of significant changes between the two point clouds and the extraction of glacier-related changes enable margin extraction. In this way, the proposed method allows glacier mapping with very high spatial resolution in scenarios where the actual glacier edge is not visible. The method is tested on two real-world datasets. Experiments show good results with relatively simple datasets. However, they demonstrate that the assumption, that geomorphological changes are primarily caused by glaciers, represents the limiting factor. Possible improved filtering methods are discussed.

2. Workflow

The following subsections describe the methods used, starting with point cloud registration, filtering the data to distinguish between glacier and non-glacier points, and finally contour extraction. Figure 1 provides a schematic overview of the process.

2.1 Registration

Multi-temporal 3D point clouds, captured by terrestrial laser scanning (TLS) and unmanned aerial vehicle (UAV) imagery, are used for glacier margin assessment. To allow for an accurate change detection, a robust point cloud registration is necessary, which excludes those parts of the point clouds from the registration process, that are showing changes between both epochs. The used registration algorithm is a supervoxel-based algorithm for identification of stable areas in deformed point clouds (Yang and Schwieger, 2023). As the transformation estimation relies on a point-to-plane iterative closest point (ICP) algorithm, a coarse registration is first necessary. This can be achieved, for example, from georeferencing, by applying a 4-point congruent set algorithm (Aiger et al., 2008) or a 3D key-point based registration pipeline (Isfort et al., 2024). Given this, both point clouds are segmented into supervoxels based on a synthetic feature distance (SFD). The SFD is the weighted sum of the distance to the nearest supervoxel starting point and a planarity criterion. The planarity criterion is represented by the normal deviation. The segmented supervoxels can be seen as roughly planar patches and are represented by their centroid and

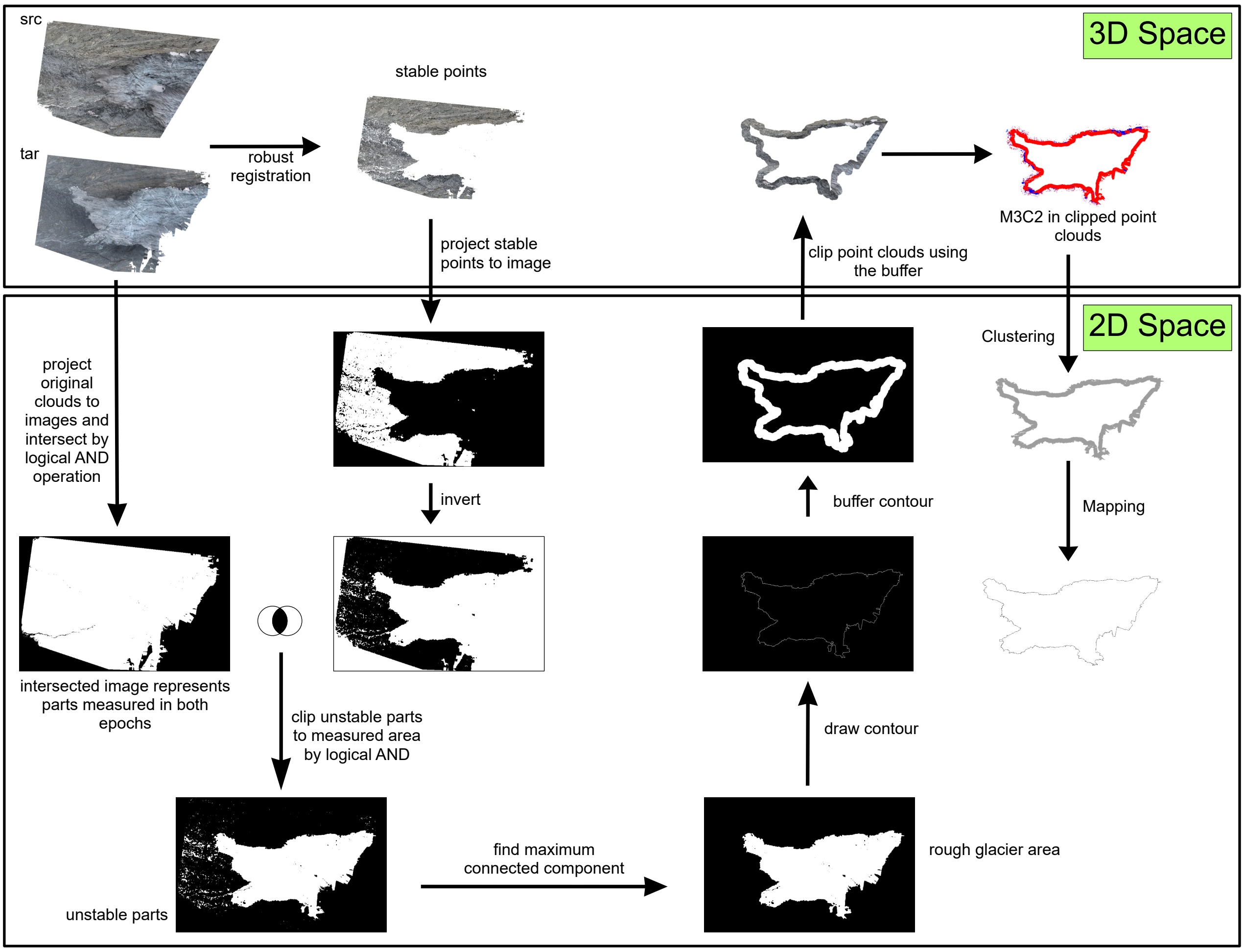

Figure 1. Schematic overview of the entire processing pipeline. In the projected images, white cells contain at least one projected point, black cells contain no points. No rasterization is used for clustering and mapping.

boundary points. These points are used to iteratively analyze, whether the supervoxel has changed by means of corresponding distances between source and target epoch, compared with a threshold. In a loop with a nested point-to-plane ICP, stable supervoxels are selected and used for transformation estimation until a convergence criterium is reached. The threshold itself converges with each iteration from a user given start value to the local minimum detectable deformation (LMDD), which is calculated as follows (Yang and Schwieger, 2023):

$$LMDD = y_p * \sqrt{\sigma^2_{BP,src} + \frac{\sigma^2_{CT,tar}}{n_{eff}}} \tag{1}$$

y_P denotes for the quantile of the normal distribution, which is set to 1.96 for the 95th percentile. $\sigma^2_{BP,src}$ and $\sigma^2_{CT,tar}$ refer to the variance of the boundary points in the source cloud and the variance of the centroids in the target cloud, respectively. n_{eff} is the number of actual measurements. $\sigma_{CT,tar}$ is calculated from the number n_{SV} of points with variance σ_i within the respective supervoxel.

$$\sigma^2_{CT,tar} = \frac{\sum_{i=1}^{n_{SV}} \sigma_i^2}{n_{SV}} \tag{2}$$

$\sigma_{CT,tar}$ is normalized by the number of effective measurements n_{eff}, where K denotes to an empirical spatial correlation factor set to 0.65.

$$n_{eff} = \frac{n_{SV}}{1 + K * (n_{SV} - 1)} \tag{3}$$

The original formulae for the LMDD calculations suggest, that the LMDD is calculated for each single supervoxel. However, a single global LMDD threshold is finally used. That's why we calculated the mean value for the fraction $\sigma^2_{CT,tar}/n_{eff}$ of all supervoxels in the target point cloud to represent the overall point cloud properties. Further, we interpreted the $\sigma_{BP,src}$ value as the single three-dimensional point variance.

The algorithm results in a final transformation matrix as well as a categorized point cloud by means of changed and unchanged supervoxels.

2.2 Change Detection and Filtering

Now given a robust fine registration, significant differences of both point clouds are searched. In a first approximate solution, the categorized data (changed/unchanged) of the registration process allows us for a rough data filtering by projecting the point cloud data to two-dimensional rasters, referred to as images. Actually, the following image based filter step isn't necessary, since information in higher resolution is given by a point cloud comparison. But this task has high computational costs compared to the proposed image projection and filtering step. Given that, the image based rough filtering can be seen as computational optimization. To do this, all points of source and target epoch are orthogonally projected onto separate binary images with same dimensions and a user-given raster cell size. White pixels represent raster cells containing at least one projected point, black pixels contain no projected points. The image plane is defined by the coordinate systems XY-plane (reasonable if given georeferenced projected coordinates) or a best fit plane. Second, both images are intersected by a pixel-wise logical AND operation to clip them to a common region in source and target point cloud.

Another image is created from the points categorized as unchanged in source point cloud. After applying a dilation to reduce the noise, the image is inverted to represent changed areas. This workaround is used instead of a direct projection of changed points, since there are changed points over the total measured area, while unchanged points are more likely only found on non-glacial areas. By projecting the unchanged points first and inverting that image, the glacial parts more clearly stand out. The inverted image is intersected with the formerly intersection of the total source and target images again by a pixel-wise logical AND operation, to clip the image of changed areas to the actually measured area. Finally, assuming the moved glacial part of the point cloud is the biggest cluster of white cells in the resulting image, the largest connected component is filtered and its contour is drawn. By re-projecting all contour pixels back to the point cloud, the rough glacier margin is filtered. Since the image based contour filtering is rather rough, a generous buffer is used for point cloud re-projection to ensure the filtered point cloud still includes the true margin for a more refined point cloud based filtering. For logical operations on images, dilation and contour extraction, OpenCV has been used (Bradski, 2000).

The clipped pair of point clouds representing the two time instances is compared using the M3C2 method, which detects points with significant change based on an empirically estimated level of detection (LOD). It considers the local point variance within a cylinder of diameter d in both point clouds ($roughness$) as well as a constant registration uncertainty (reg) (Lague et al., 2013). The registration uncertainty is estimated using the previously identified unchanged parts of the point clouds. For each stable supervoxel in the source point cloud, the nearest point to its centroid serves as core point for a M3C2 distance calculation between source and target point cloud. The distances standard deviation estimates the global registration uncertainty. In contrast to the originally proposed LOD computation, a third term is added. It represents slight changes caused by erosion (ero) of loose ground, for example gravel and sands. By this, the sensitivity is reduced, which might be necessary in some scenarios, to avoid a systematic glacier outline overestimation.

$$LOD_{95\%}(d) = \pm 1.96\,(roughness + reg + ero) \tag{4}$$

with

$$roughness = \sqrt{\frac{\sigma_1(d)^2}{n_1} + \frac{\sigma_2(d)^2}{n_2}} \tag{5}$$

where

$$\begin{aligned} d &= cylinder\ diameter \\ \sigma_i(d)^2 &= variance\ in\ normal\ direction\ within\ d \\ n_i &= number\ of\ points\ within\ d \end{aligned}$$

Next, the significantly changed points are clustered using the DBSCAN algorithm (Ester et al., 1996). Therefore, the point set is projected onto a mapping plane. The XY-plane is reasonable given georeferenced and projected coordinates. Large clusters are considered as glacial induced movements, smaller clusters as non-glacial. The smallest cluster of changed points considered as glacial induced is defined as the cluster c_i with the largest leap in the sorted list of log-scaled cluster sizes by number of points.

$$smallest\,glacial\,cluster = \max_{i=2,\ldots,n} log\left(\frac{c_i}{c_{i-1}}\right) \tag{6}$$

All clusters with point numbers equal or larger than the smallest glacial cluster are considered as part of the glacier to be mapped.

2.3 Outline Extraction

The set of isolated, significantly changed, projected glacier points is used for margin mapping. First, an approximation for the glacier outline is calculated based on the swinging arm algorithm: Starting from one dimension's maximum or minimum point, an arm of user defined length is swung clockwise until a new point is reached. This new vertex serves as starting point for the second iteration. This way, the algorithm finds the contour of the given set of points, until the loop closes reaching the start point (Galton and Duckham, 2006). The results of the swinging arm algorithm have a medium level of detail, compared to a low level of detail given by, e.g., a convex hull algorithm.

To further refine the outline, a second concave hull algorithm based on the one proposed by (Park and Oh, 2012) is applied. Given the coarse swinging arm outline, each edge is optimized by searching a valid new vertex point to split the edge and thereby refine the outline. A candidate point is searched in a maximum radius to reduce the computational costs and has to fulfill some conditions to be considered valid:

1. Candidate is not a vertex of another edge segment
2. Projection of the candidate falls on the current edge segment
3. Candidate must be inside the hull
4. New pair of edges must not intersect existing edges

Out of all valid points, the one with the maximum angle between the vectors $\overrightarrow{CV_1}$ and $\overrightarrow{CV_2}$ with candidate point C and existing vertices V_1, V_2 is chosen as new vertex point. Finally the edge segment is split, if the new vertex is closest by orthogonal distance to the edge segment to be split compared to the following and previous edge segments.

In the original algorithm by (Park and Oh, 2012), the candidate with the shortest distance to a vertex is chosen. With our angle based approach we intend a faster convergence and a more homogeneous outline, as the finally chosen candidate point tends to lie more centered on the edge to be split.

3. Evaluation Data

3.1 Bøverbreen - Norway

For evaluation, the proposed workflow is used to map the glacier margins in various datasets. The Bøverbreen glacier (Jotunheimen, Norway) has been measured on a yearly basis from 2022 to 2025. Using UAV imagery with a flight pattern of oblique images and cross-grid nadir images, between 385 and 1758 images have been taken each year with an approximately ground sampling distance of 2 cm. The UAV's direct georeferencing in combination with some ground control points allows for a georeferencing of the final products within a centimeter accuracy in the ETRS89/UTM32N reference system. Besides orthophotos, 3D point clouds have been calculated within Agisoft Metashape. To reduce the computational costs and ensure a high data quality, all point clouds have been filtered with a minimum confidence threshold and subsampled with a voxel based filter of 5 cm cube size. Finally, a statistical outlier filter is applied using CloudCompare, to eliminate leftover false reconstructions. Table 1 gives a brief overview on the data. Further details on the UAV image data acquisition and processing can be found in (Elias et al., 2024).

year	image #	mean error CP	point #
		cm	$*10^6$
2022	385	2.0	39.9
2023	918	2.2	43.1
2024	1758	1.9	63.5
2025	1179	2.0	37.2

Table 1. Brief overview of the UAV image datasets for the Bøverbreen glacier. CP stands for control points. The point numbers refer to the size after applying the filtering process.

The mapped glacier lies in a valley whose northern and southern flanks are lined with exposed rock faces. The area is covered with debris and stones of different sizes, and in parts also with loose gravel and sand. The area shows clear signs of erosion (see figure 2). On the glacier itself, only small areas at the terminus are covered with debris. The visible ice of the Bøverbreen glacier allows for a manual assessment of the glacier margins using the orthophoto mosaics from the individual epochs. The manual assessed margins serve as a reference for the proposed algorithm (see section 4.1).

3.2 Hochebenkar - Austria

Another data set used for the evaluation is a pair of point clouds that was obtained by terrestrial laser scanning of the Äußeres Hochebenkar rock glacier in Austria in the years 2015 and 2017 (Pfeiffer et al., 2019). Both epochs are georeferenced in the ETRS89/UTM32N. As can be expected for TLS data and in contrast to the UAV datasets of the Bøverbreen, both clouds have a strongly varying point density as well as gaps caused by occlusions. The glacier is covered by larger rocks and debris, as is the surrounding area. Based on (Brardinoni et al., 2026), the glacier margin can be estimated using the elevation profile of the terrain. The glacier literally lies on the slope and is clearly recognizable as an elevation in the elevation profile. The glacier's front and flanks feature a distinct edge with a fairly steep slope, which can be used to roughly estimate the reference glacier boundary in 2015 (see figure 3).

Figure 2. Views on the Bøverbreen's edge, showing characteristic erosion of loose rocks, gravel and sands besides the margin to detect.

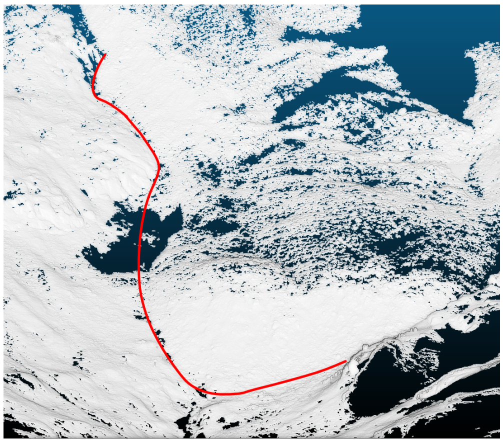

Figure 3. TLS point cloud of the Hochebenkar rock glacier in 2015 with roughly guessed outline based on the area's elevation profile.

4. Results and Discussion

4.1 Bøverbreen - Norway

Data processing followed the methods presented in section 2. The initial supervoxel resolution was set to 0.5 m. The LMDD for all registered pairs was approximately 5 cm. Therefore, the single point standard deviation σ_i and the boundary points standard deviation $\sigma_{BP,src}$ were set to 2 cm in all calculations. This is derived from an empirically estimated point standard deviation relative to an adjusted plane in flat regions of the point clouds. The registration errors, in comparison with the registration errors solely based on the georeferencing, can be seen in table 2. It appears that the registration error has improved by up to 2.5 cm.

For rough outline filtering, the clouds have been projected to the XY-plane, since the data is already in a projected reference system. The raster cell size was set to 0.5 m. The total point clouds of both epochs were clipped using the contour with a buffer of approximately 15 m. Table 3 shows the parameters used for the M3C2 distance calculation. The registration error has been assessed from the stable parts of the point clouds.

https://doi.org/10.5194/isprs-archives-XLIX-B2-2026-1035-2026

years	registration error georef.	registration error SV-ICP
	cm	cm
22-23	1.1	0.7
23-24	3.1	0.6
24-25	1.5	1.0

Table 2. Comparison of registration results for registration by georeferencing and supervoxel based registration. Registration quality estimated as standard deviation of M3C2 distances in flat areas (see section 2.2).

Erosion compensation was set to 1 cm, compensating for smaller erosions of gravel and sand. The resulting median thresholds for distances to be considered as significant lie between 4.7 cm and 5.4 cm. For DBSCAN-Clustering, a radius of 0.3 m and a minimum point number of 50 points has been used.

years	median roughness	registration error	median LOD
	cm	cm	cm
22-23	0.7	0.7	4.7
23-24	0.8	0.6	4.8
24-25	0.8	1.0	5.4

Table 3. M3C2 parameters. Term for erosion compensation was constantly set to 1 cm.

Finally, the outlines were calculated using the swinging arm and concave hull algorithm. In the following, the results of both algorithms are compared to the manually drawn outlines from the orthophotos serving as references. Figure 4 shows the reference outlines and the estimated outlines.

The visual inspection shows generally good results for both algorithms, with more generalized outlines from the swinging arm, as expected. For a more objective comparison, all concave hull outlines have been closed to polygons and their areas have been calculated. Each estimated polygon is compared with the corresponding reference polygon by clipping operations, to reveal overestimated and underestimated glacial areas. Table 4 shows the results. Relative errors set the net area difference in ratio to the total area of the reference polygon. Please note that the mapped area was expanded in 2024.

Table 4 shows a generally small and consistent error in total mapped glacier area of 3.4 % in maximum. It also shows a clear trend in overestimating the glacier outline, which is expected due to the sensitivity to any kind of morphology change.

year	mapped area	overest. +	underest. -	net. diff	rel. diff
	m^2	m^2	m^2	m^2	%
2022	31789.65	905.02	35.96	869.06	2.7
2023	27504.08	972.45	27.40	945.05	3.4
2024	33458.88	648.57	29.20	619.37	1.9

Table 4. Boverbreen concave hull glacier margins compared to reference outlines.

Considering the length of the reference glacier margin, the estimated margin deviates from the reference by an average of approximately 0.8 m, 1.0 m, and 0.6 m in 2022, 2023, and 2024, respectively. However, the general difference is smaller. Instead, there are some areas with huge differences. For example, figure 5 shows the glacier front in 2023 with the estimated and reference outlines. The area is characterised by loose gravel and glacial meltwater and is therefore particularly susceptible to erosion. Consequently, the outline is overestimated, as the

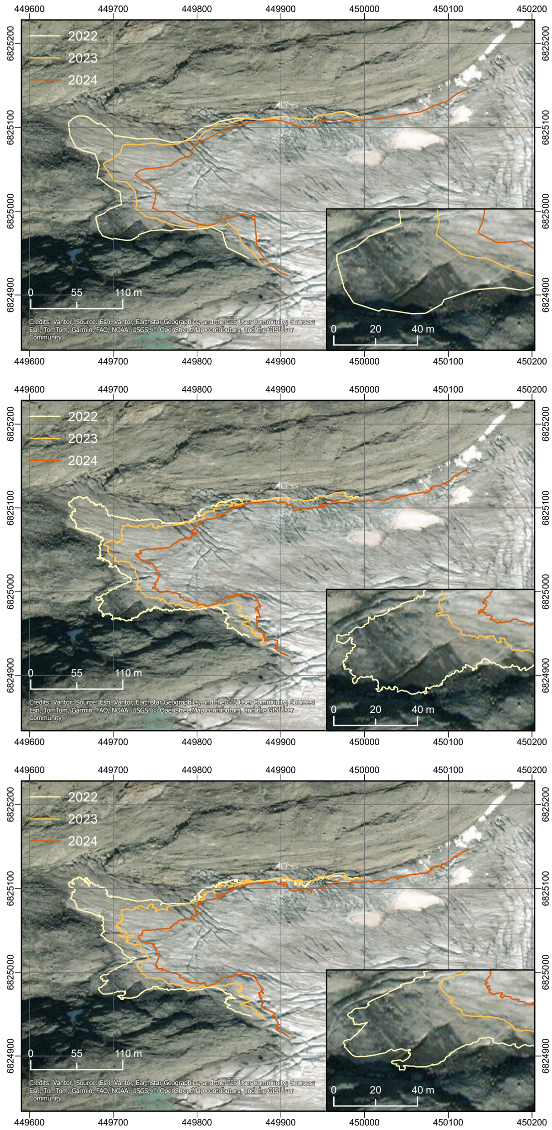

Figure 4. Top: Swinging Arm outlines, Center: Concave Hull outlines, Bottom: Reference outlines of the Bøverbreen glacier manually drawn in the respective orthophotos; CRS: ETRS89/UTM32N

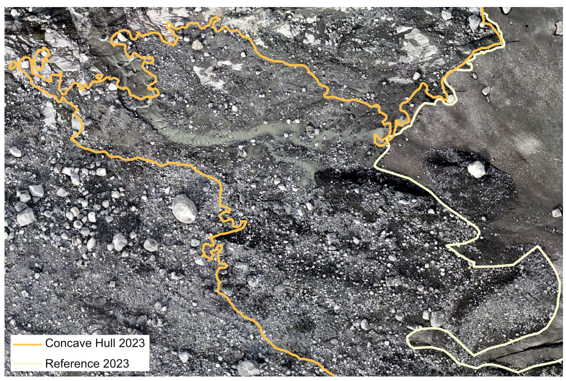

Figure 5. Front of the Bøverbreen glacier in 2023. The image illustrates the sensitivity to any kind of morphological change, such as erosion.

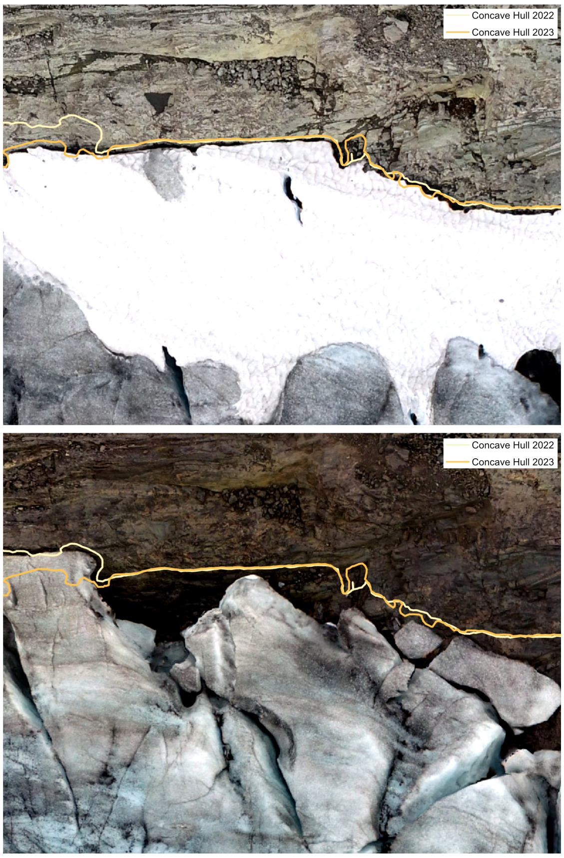

Figure 6. Section of the Bøverbreen outline in 2022 (bottom) and 2023 (top). The outline estimation for 2022 is influenced by a snowfield in 2023.

simple differences in the point cloud data due to erosion cannot be distinguished from changes caused by glaciers. A second example is given in figure 6. A section of the outline is shown for the years 2022 and 2023. A change in elevation due to a snowfield in 2023 has influenced the estimate of the glacier's outline in 2022. Subsequently, the outlines for 2022 and 2023 are essentially the same for both years, which most likely does not reflect reality, as the glacier has retreated in all other areas. Furthermore, the results show that individual larger stones, displaced by erosion, often influence the determination of the glacier outline. Overall, sensitivity to any kind of morphological change is very high.

4.2 Hochebenkar - Austria

The dataset Äußeres Hochebenkar was processed using the same workflow as for the Bøverbreen datasets. Figure 7 shows the estimated and reference contours for the year 2015. Compared to the Bøverbreen datasets, the differences between the two contours are greater. The net deviation in the mapped glacier area is 2312.99 m^2, which corresponds to a relative deviation of 9.4 % for a total mapped area of 24529.72 m^2.

However, it must be noted that the quality of the reference is also less accurate, as it is estimated solely on the basis of the elevation profile by a non-expert operator. Another reason is data quality. Gaps and irregular point density have a significant impact on cluster formation when using the density-based DBSCAN algorithm. The radius parameter for DBSCAN had to be set quite high (1.5 m) to prevent large parts of the glacier from being excluded. As a result, however, many smaller

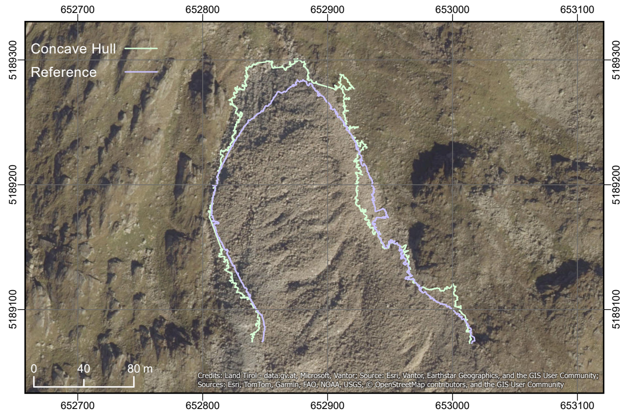

Figure 7. The map shows the estimated and reference outlines of the Äußeres Hochebenkar rock glacier for 2015; CRS: ETRS89/UTM32N

clusters near the glacier are merged into the glacier clusters. Furthermore, the area appears to exhibit higher geomorphological activity, leading to significantly larger distances between the two clouds near the presumed edge. Overall, assuming an approximately correct reference contour, the glacier cannot be filtered out as clearly.

5. Conclusion

The results demonstrate that the proposed method achieves good results provided that the dataset contains little noise or that the filtering is performed robustly. Tests in both scenarios reveal that the greatest challenge lies in distinguishing glacier points from non-glacier points. Currently, glacier points are filtered out solely based on the point density of significantly changed points, which, as the examples shown demonstrate, proves to be insufficiently reliable as the sole criterion. Any changes in non-glaciated areas, for example due to precipitation or erosion, influence edge extraction and tend to lead to an overestimation of the glaciated area. When considering events such as large displaced rocks and snowfields, this is not simply a matter of the threshold value. Furthermore, the dependence on data quality is currently quite high. Point density and gaps have a strong influence on the results. The experiments also show that evaluating the results is difficult without a true reference.

6. Future Work

In consideration of the aforementioned drawbacks, several tasks arise for future work. First, we will investigate data simulations to generate real reference data that will enable a systematic verification of our methods and results. Our filtering methods will be updated, for example by incorporating a state-of-the-art point cloud distance algorithm, and additional features will be taken into account, such as surface motion vectors. Prior knowledge of glacier motion and shape, such as slope direction and elevation profile, should be incorporated, as well as a neighborhood analysis of the changed point behavior, assuming that glacier motion is less affected by noise compared to morphological changes caused by erosion. Finally, when incorporating additional features, multidimensional clustering must be considered.

Acknowledgement

We kindly thank PhD Liss Marie Andreassen and the Jotunheimen National Park Management for supporting and authorising the UAV flights and Kartverket for providing the CPOS service.

References

Aiger, D., Mitra, N. J., Cohen-Or, D., 2008. 4-points congruent sets for robust pairwise surface registration. *ACM SIGGRAPH 2008 Papers*, SIGGRAPH '08, Association for Computing Machinery, New York, NY, USA.

Avian, M., Bauer, C., Schlögl, M., Widhalm, B., Gutjahr, K.-H., Paster, M., Hauer, C., Frießenbichler, M., Neureiter, A., Weyss, G., Flödl, P., Seier, G., Sulzer, W., 2020. The Status of Earth Observation Techniques in Monitoring High Mountain Environments at the Example of Pasterze Glacier, Austria: Data, Methods, Accuracies, Processes, and Scales. *Remote Sensing*, 12(8). https://www.mdpi.com/2072-4292/12/8/1251.

Bertone, A., Jones, N., Mair, V., Scotti, R., Strozzi, T., Brardinoni, F., 2024. A climate-driven, altitudinal transition in rock glacier dynamics detected through integration of geomorphological mapping and synthetic aperture radar interferometry (InSAR)-based kinematics. *The Cryosphere*, 18(5), 2335–2356. https://tc.copernicus.org/articles/18/2335/2024/.

Bradski, G., 2000. The OpenCV Library. *Dr. Dobb's Journal of Software Tools*.

Brardinoni, F., Vivero, S., Barboux, C., Bodin, X., Cicoira, A., Echelard, T., Hu, Y., Jones, N., Lambiel, C., MacDonell, S., Pellet, C., Rouyet, L., Ruiz, L., Schaffer, N., Wehbe, M., Delaloye, R., 2026. RGIK guidelines for compiling consistent rock glacier inventories. *Geomorphology*, 492, 110050. https://doi.org/10.1016/j.geomorph.2025.110050.

Elias, M., Isfort, S., Eltner, A., Maas, H.-G., 2024. UAS Photogrammetry for Precise Digital Elevation Models of Complex Topography: A Strategy Guide. *ISPRS Annals of the Photogrammetry, Remote Sensing and Spatial Information Sciences*, X-2-2024, 57–64. https://isprs-annals.copernicus.org/articles/X-2-2024/57/2024/.

Ester, M., Kriegel, H.-P., Sander, J., Xu, X., 1996. A density-based algorithm for discovering clusters in large spatial databases with noise. *Proceedings of the Second International Conference on Knowledge Discovery and Data Mining*, KDD'96, AAAI Press, 226–231.

Galton, A., Duckham, M., 2006. What is the region occupied by a set of points? *International conference on geographic information science*, Springer, 81–98.

Gardner, A. S., Moholdt, G., Cogley, J. G., Wouters, B., Arendt, A. A., Wahr, J., Berthier, E., Hock, R., Pfeffer, W. T., Kaser, G., Ligtenberg, S. R. M., Bolch, T., Sharp, M. J., Hagen, J. O., van den Broeke, M. R., Paul, F., 2013. A Reconciled Estimate of Glacier Contributions to Sea Level Rise: 2003 to 2009. *Science*, 340(6134), 852-857. https://www.science.org/doi/abs/10.1126/science.1234532.

Isfort, S., Elias, M., Maas, H.-G., 2024. Development and Evaluation of a Two-Staged 3D Keypoint Based Workflow for the Co-Registration of Unstructured Multi-Temporal and Multi-Modal 3D Point Clouds. *ISPRS Annals of the Photogrammetry, Remote Sensing and Spatial Information Sciences*, X-2-2024, 113–120. https://isprs-annals.copernicus.org/articles/X-2-2024/113/2024/.

Lague, D., Brodu, N., Leroux, J., 2013. Accurate 3D comparison of complex topography with terrestrial laser scanner: Application to the Rangitikei canyon (N-Z). *ISPRS Journal of Photogrammetry and Remote Sensing*, 82, 10–26.

Oerlemans, J., 1994. Quantifying Global Warming from the Retreat of Glaciers. *Science*, 264(5156), 243-245. https://www.science.org/doi/abs/10.1126/science.264.5156.243.

Park, J.-S., Oh, S.-J., 2012. A New Concave Hull Algorithm and Concaveness Measure for n-dimensional Datasets. *Journal of Information Science & Engineering*, 28(3).

Pfeffer, W. T., Arendt, A. A., Bliss, A., Bolch, T., Cogley, J. G., Gardner, A. S., Hagen, J.-O., Hock, R., Kaser, G., Kienholz, C., et al., 2014. The Randolph Glacier Inventory: a globally complete inventory of glaciers. *Journal of Glaciology*, 60(221), 537–552.

Pfeiffer, J., Höfle, B., Hämmerle, M., Zahs, V., Rutzinger, M., Scaioni, M., Lindenbergh, R., Oude Elberink, S., Pirotti, F., Bremer, M., Wujanz, D., Zieher, T., 2019. Terrestrial laser scanning data of the Äußeres Hochebenkar rock glacier close to Obergurgl, Austria acquired during the Innsbruck Summer School of Alpine Research.

Robson, B. A., Bolch, T., MacDonell, S., Hölbling, D., Rastner, P., Schaffer, N., 2020. Automated detection of rock glaciers using deep learning and object-based image analysis. *Remote Sensing of Environment*, 250, 112033. https://doi.org/10.1016/j.rse.2020.112033.

Shangguan, D. H., Bolch, T., Ding, Y. J., Kröhnert, M., Pieczonka, T., Wetzel, H. U., Liu, S. Y., 2015. Mass changes of Southern and Northern Inylchek Glacier, Central Tian Shan, Kyrgyzstan, during ∼1975 and 2007 derived from remote sensing data. *The Cryosphere*, 9(2), 703–717. https://tc.copernicus.org/articles/9/703/2015/.

Ulrich, V., Williams, J. G., Zahs, V., Anders, K., Hecht, S., Höfle, B., 2021. Measurement of rock glacier surface change over different timescales using terrestrial laser scanning point clouds. *Earth Surface Dynamics*, 9(1), 19–28. https://esurf.copernicus.org/articles/9/19/2021/.

Yang, Y., Schwieger, V., 2023. Supervoxel-based targetless registration and identification of stable areas for deformed point clouds. *Journal of Applied Geodesy*, 17(2), 161–170. https://doi.org/10.1515/jag-2022-0031.